

SPE-210461-MS

Multiscale Carbonate Rock Reconstruction Using a Hybrid WGAN-GP and Super-Resolution

Zhen Zhang and Yiteng Li, King Abdullah University of Science and Technology; Marwah AlSinan, Saudi Aramco; Xupeng He, King Abdullah University of Science and Technology; Hyung Kwak, Saudi Aramco; Hussein Hoteit, King Abdullah University of Science and Technology

Copyright 2022, Society of Petroleum Engineers DOI [10.2118/210461-MS](https://doi.org/10.2118/210461-MS)

This paper was prepared for presentation at the 2022 SPE Annual Technical Conference and Exhibition held in Houston, Texas, USA, 3 - 5 October 2022.

This paper was selected for presentation by an SPE program committee following review of information contained in an abstract submitted by the author(s). Contents of the paper have not been reviewed by the Society of Petroleum Engineers and are subject to correction by the author(s). The material does not necessarily reflect any position of the Society of Petroleum Engineers, its officers, or members. Electronic reproduction, distribution, or storage of any part of this paper without the written consent of the Society of Petroleum Engineers is prohibited. Permission to reproduce in print is restricted to an abstract of not more than 300 words; illustrations may not be copied. The abstract must contain conspicuous acknowledgment of SPE copyright.

Abstract

The X-ray micro-Computed Tomography (μ -CT) is the primary tool for digital rock imaging, which provides the foundation for numerically studying petrophysical properties of reservoir rocks at the pore scale. However, the finite resolution of μ -CT imaging cannot capture the micro-porosity at the sub-micrometer scale in carbonate rocks. The tradeoff between the resolution and field of view (FOV) is a persisting challenge in the industry. The machine-learning-based single-image super-resolution techniques has rapidly developed in the past few years. It is becoming a promising approach to "super-resolve" low-resolution carbonate rock images. In this study, we present a fast super-resolution generative adversarial network to enhance the image resolution of carbonate rocks. A pre-trained VGG network is implemented to extract important high-level features, from which the perceptual similarity is evaluated between the generated and ground-truth images. The novelty of this study is two-fold. First, the generator is significantly simplified with a fast super-resolution convolutional neural network. On the other hand, the spatial and channel squeeze-and excitation block is applied to recalibrate nonlinear feature mapping so that the quality of super-resolved images is promising even with much fewer residual blocks.

To quantify the quality of the super-resolution images, we compare difference maps between the generated and ground-truth images. Numerical results indicate that the proposed network shows excellent potential in enhancing the resolution of heterogeneous carbonate rocks. In particular, the pixel errors are minor, and the super-resolution images exhibit clear and sharp edges and dissolved mineral texture. This study provides a novel machine-learning-based method using a simple generative adversarial network with squeeze and excitation blocks to super-resolve μ -CT images of carbonate rocks.

Keywords: Carbonate rocks, Digital rock imaging, Super-resolution generative adversarial network, Spatial and channel squeeze-and-excitation block, VGG19 network

Introduction

Digital rocks offer a platform to numerically evaluate the petrophysical properties of reservoir rocks and simulate fluid flow mechanisms (Andrä et al., 2013; Ferrand & Celia, 1992; Mostaghimi et al., 2013; Y. Wang & Sun, 2021). As the most commonly used imaging tool, μ -CT can resolve porous structures down to a few micrometers, which is sufficient enough to characterize rocks like sandstone (Coenen et al., 2004; Flannery et al., 1987). On the other hand, scanning electron microscopy surpasses μ -CT in imaging the micro-porosity at the submicron scale that is pervasive in carbonate rocks, but it has a much smaller field of view. The contradiction between resolution and field of view has haunted the digital rock physics community for years, as it is highly demanding to have high-resolution 3D digital rocks to effectively characterize the multiscale nature of carbonate rocks. Therefore, super-resolution is a promising approach to address this problem by increasing image details and texture while retaining a large field of view.

Deep learning techniques have been successfully applied in many fields in recent years. Specifically, the deep learning algorithms can be categorized into four different types: the ANN focus on the value to value problems, applications like optimization of gas injection (He et al., 2021c), prediction of mud loss (Albattat et al., 2022), estimation of fracture permeability (He et al., 2021), forecasting of CO₂ storage capacity (He et al., 2022), and physics informed neural network (Alhubail et al., 2022) show good performance; the LSTM can deal with time-series problems and has been successfully deployed in the field of history matching (Santoso et al., 2021), detection of CO₂ leakage rate (He et al., 2021a), and oil production forecasting (Tadjer et al., 2021); CNN can solve the image to value problems like the upscaling technics (He et al., 2021b; He et al., 2020; Santoso et al., 2019); and GAN can be applied on the image to image problems like digital rock reconstructions (Li et al., 2022). The tremendous success of the machine learning approach inspires us to solve the super-resolution problem in a data-driven manner.

In the field of super-resolution, the single-image super-resolution methods rapidly developed in the computer vision research community (Dong et al., 2015, 2016; Ledig et al., 2017; Lim et al., 2017; X. Wang et al., 2018). It draws increasing attention from the petroleum industry and has been applied in digital rock imaging. Wang et al. (2019) used a Super-Resolution Convolutional Neural Network (SRCNN) to increase the resolution of μ -CT images. Their super-resolved images captured the edge sharpness and suppressed image noises. They extended to combining SRCNN with the generative adversarial network (GAN), resulting in a super-resolution GAN (SRGAN), which achieved good performance in super-resolution similarly (Wang et al., 2020). Chen et al. (2020) used the CycleGAN-based super-resolution to produce high resolution and high field of view images. Bai et al. (2020a) performed the super-resolution process using a CNN combined with the bicubic interpolation method. They also used a Fast Super-Resolution Convolutional Neural Network (FSRCNN) to enhance the resolution of digital rock images with less time (Bai et al., 2020b).

Both SRCNNs and SRGANs have been successfully applied in the super-resolution of μ -CT images. Their success heavily relies on the complex network architecture with many residual blocks, as well as skip connections that are helpful to reduce the complexity of the training process. The objective of this study attempts to develop a simple and fast super-resolution generative adversarial network without much compromise in accuracy. For this purpose, we use the FSRCNN as the generator network and replace the nonlinear mapping layers with three residual blocks. The spatial and channel squeeze-and-excitation block is utilized to recalibrate feature flow and amplify high-frequency details. In addition, we adopt the Wasserstein GAN with gradient penalty to stabilize the training process. Benefiting on this technology, the proposed network successfully captures detailed structures of the carbonate rocks, including sharp edges and dissolved mineral texture, with much fewer residual blocks.

Methods

Fast super-resolution generative adversarial network (FSRGAN)

As Goodfellow et al. (2014) proposed the generative adversarial network, numerous GAN variants have been developed and extensively applied in digital rock physics (Wang et al., 2021), including image denoising (Niu et al., 2021), image super-resolution (Chen et al., 2020; Wang et al., 2020), image segmentation (Karimpouli & Tahmasebi, 2019; Niu et al., 2020), and image reconstruction (Li et al., 2022; Mosser et al., 2017; Shams et al., 2020; Wang et al., 2018). Regardless of the architectural complexity of GANs, they typically include two critical components: the generator (G) attempts to create images as real as possible, while the discriminator (D) distinguishes the real and fake images. This two-player game can be reformulated as a min-max optimization problem. Ideally, the discriminator cannot differentiate between real and fake images at equilibrium.

In this study, we create the FSRGAN, as an alternative to the SRGAN (Ledig et al., 2017), by replacing the generator network with the FSRCNN (Dong et al., 2016). This leads to two pronounced advantages. First, the SRGAN has 16 residual blocks with many to-be-optimized parameters. The hourglass-shape FSRCNN significantly reduces the number of parameters and eases the training process. On the other hand, the FSRCNN uses the deconvolution layer at the end of the network, which is beneficial for transfer learning across different upscaling factors.

The generator retains the overall structure of FSRCNN, except the nonlinear mapping layers between shrinking and expanding steps, are substituted by three residual blocks with skip connections. Each residual block has two convolution layers, consisting of 16 filters with 3×3 kernels, followed by two Parametric Rectified Linear Unit (PReLU) layers. Batch normalization layers have been removed from SRCNNs as they increase the computational complexity and memory consumption. More importantly, it has been demonstrated harmful to training. In addition, the discriminator adopts a fully convolutional network, and each convolution layer is followed by a leaky ReLU layer with the negative slope coefficient being 0.2. The detailed structures of the generator and discriminator are shown in Figure 1.

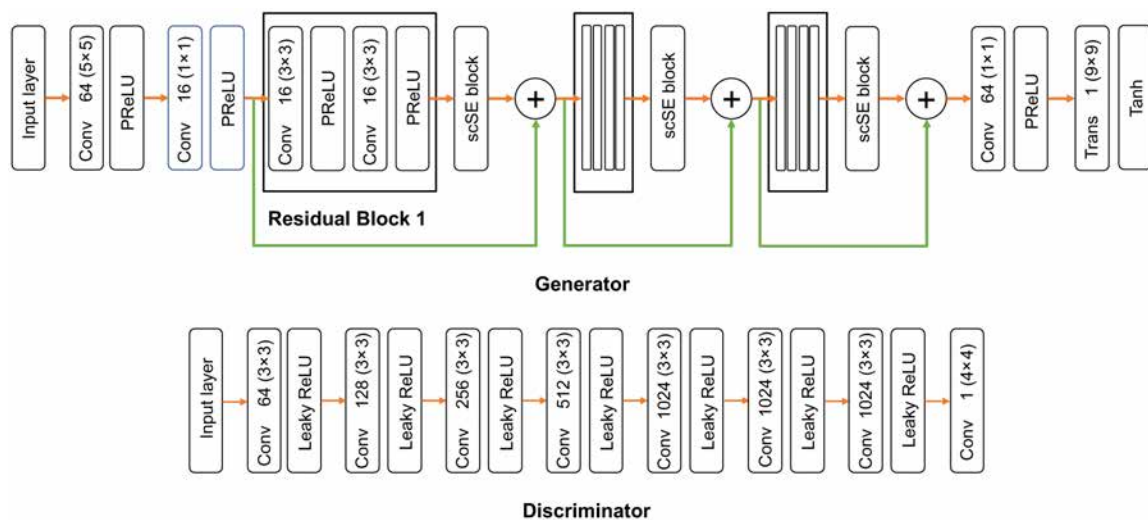


Figure 1—Schematic diagram of the generator and discriminator of the FSRGAN, modified from Ledig et al. (2017).

Spatial and channel squeeze-and-excitation (scSE) block

The (spatial) squeeze and channel excitation (cSE) block succeeded in improving the performance of CNNs by explicitly recalibrating the channel-wise feature responses (Hu et al., 2018)(Hu et al., 2018)(Hu et al., 2018). Inspired by this, Roy et al. (2018) proposed the (channel) squeeze and spatial excitation (sSE) block to enhance spatial encoding adaptively. They obtained striking improvements in segmentation performance

by jointly utilizing the cSE and sSE blocks. This combined block is called the spatial and channel excitation block, which is used in this study to assist gradient flows along both spatial and channel dimensions. As the name implies, the cSE block squeezes the spatial information using a global average pooling layer and generates a vector

$$\mathbf{z} = \frac{1}{H \times W} \sum_i^H \sum_j^W \mathbf{u}(i, j), \quad (1)$$

where $\mathbf{u} \in R^{H \times W}$ is the input feature map, H and W is the number of pixels in the height and width dimensions. The vector is then transformed using,

$$\hat{\mathbf{z}} = \mathbf{W}_1(\delta(\mathbf{W}_2 \mathbf{z})), \quad (2)$$

where $\mathbf{W}_1 \in R^{C \times \frac{C}{r}}$ and $\mathbf{W}_2 \in R^{C \times \frac{C}{r}}$ represent two fully connected layers, r indicates the bottleneck in the channel-wise excitation, and $\delta(\cdot)$ represents the ReLU activation function. The channel excitation operation can be defined as,

$$\hat{\mathbf{U}}_{\text{cSE}} = [\sigma(\hat{z}_1) \mathbf{u}_1, \sigma(\hat{z}_2) \mathbf{u}_2, \dots, \sigma(\hat{z}_C) \mathbf{u}_C] \quad (3)$$

On the other hand, the sSE block aims to squeeze the channels and activate the spatial information, and the spatial excitation can be expressed as,

$$\hat{\mathbf{U}}_{\text{sSE}} = [\sigma(q_{1,1}) \mathbf{u}^{1,1}, \dots, \sigma(q_{i,j}) \mathbf{u}^{i,j}, \dots, \sigma(q_{H,W}) \mathbf{u}^{H,W}] \quad (4)$$

where $\mathbf{u}_{i,j}$ represents the spatial location with $i \in \{1, 2, \dots, H\}$ and $j \in \{1, 2, \dots, W\}$, $q_{i,j}$ is a linear combination of all the pixels along the channel dimension. It is then fed into the sigmoid function, rescaling to (0,1) to represent the relative importance of this particular location. There are four strategies to combine the complementary information from cSE and sSE blocks: max-out, addition, multiplication, and concatenation (Roy et al., 2018). In this study, the elementwise max-out operator is used to jointly recalibrate the input in spatial and channel dimensions

$$\hat{\mathbf{U}}_{\text{csSE}}(i, j, c) = \max(\hat{\mathbf{U}}_{\text{cSE}}(i, j, c), \hat{\mathbf{U}}_{\text{sSE}}(i, j, c)). \quad (5)$$

Figure 2 illustrates the structure of the scSE block.

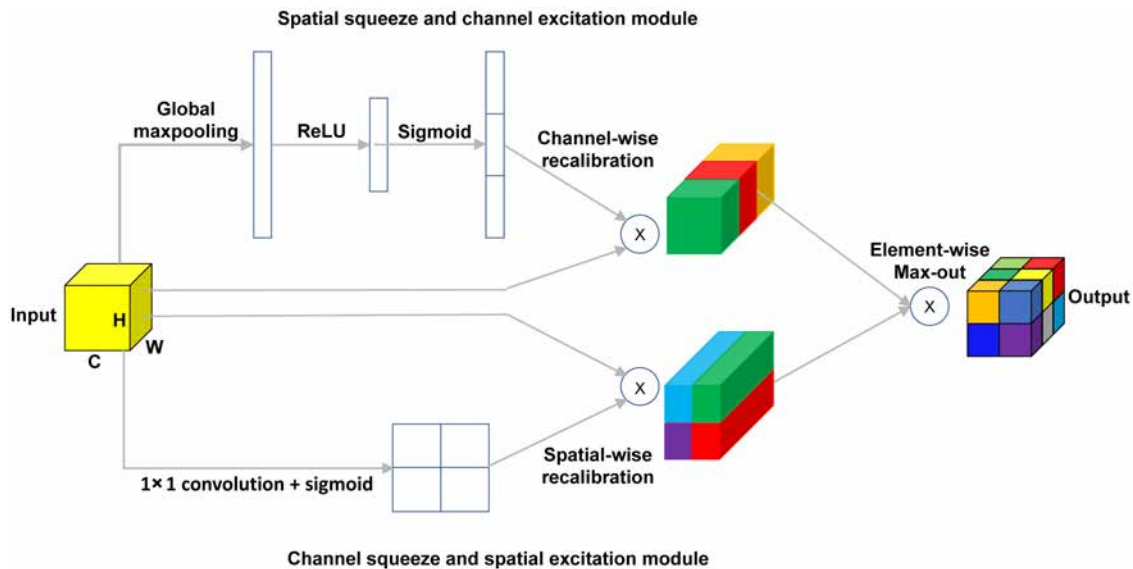


Figure 2—Schematic diagram of the scSE block, modified from Roy et al. (2018).

Perceptual loss

Instead of encouraging the pixel match between the generated super-resolution images and the ground-truth images, it is more desirable to have a perceptual similarity modeled by a loss function. For this purpose, [Johnson et al. \(2016\)](#) proposed using a pre-trained VGG network to extract high-level features. The key idea is that pre-trained CNNs for image classification tasks have already learned to encode the perceptual information. The perceptual similarity is evaluated using the VGG19 network, and the perceptual loss is defined by

$$L_{VGG} = \sum \sum [\phi_{ij}(I^{GT}) - \phi_{ij}(G(I^{input}))]^2, \quad (6)$$

where ϕ_{ij} represents the feature map extracted from the j^{th} convolution layer before the i^{th} max-pooling layer in the VGG19 network. We calculate the perceptual loss using the feature map extracted from the 5th convolution layer prior to the 4th max-pooling layer, as [Wang et al. \(2020\)](#) did in their work.

Loss function

To effectively train the proposed FSRGAN, the loss function of the generator, L_G , has three components,

$$L_G = \beta_1 L_{adv} + \beta_2 L_{VGG} + \beta_3 L_1, \quad (7)$$

where L_{adv} is the adversarial loss, L_{VGG} is the perceptual loss modeled by a VGG19 network, and the last term is the L_1 loss. Specifically, the adversarial loss is written as,

$$L_{adv} = - \sum_{i=1}^m D[G(I_i^{input})], \quad (8)$$

where m denotes the batch size, I_i^{input} is the input low-resolution μ -CT image, while $G(I_i^{input})$ is the generated super-resolution image. We use the L_1 loss to evaluate the pixel-wise difference

$$L_1 = \frac{\sum_{i=1}^N |SR_i - HR_i|}{N}, \quad (9)$$

with N being the total number of pixels of the super-resolution/high-resolution image. $\beta_1, \beta_2, \beta_3$ are the weights to balance the above loss terms, where $\beta_1 = 1, \beta_2 = 250$, and $\beta_3 = 12.5$ in this study.

Proposed workflow

The proposed super-resolution imaging process consists of three steps, as shown in [Figure 3](#): 1) dataset preparation, 2) network training, and 3) quality assessment. We briefly describe each step below.

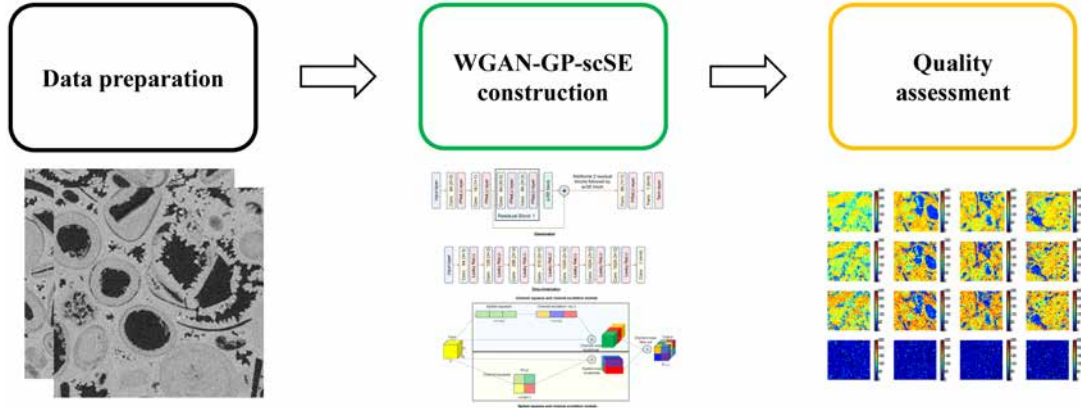


Figure 3—Illustration of the proposed workflow.

Step 1 – Data preparation: the proposed FSRGAN is trained based on the carbonate rock images, a subset of the DeepRock-SR-2D dataset (Wang et al., 2019). This dataset contains 4000 high-resolution (500×500) and 4000 low-resolution (125×125) μ -CT images. It is split into the training, validation, and testing sets with a ratio of 8:1:1. Figure 4 displays low-resolution (first row) and high-resolution (second row) images, respectively.

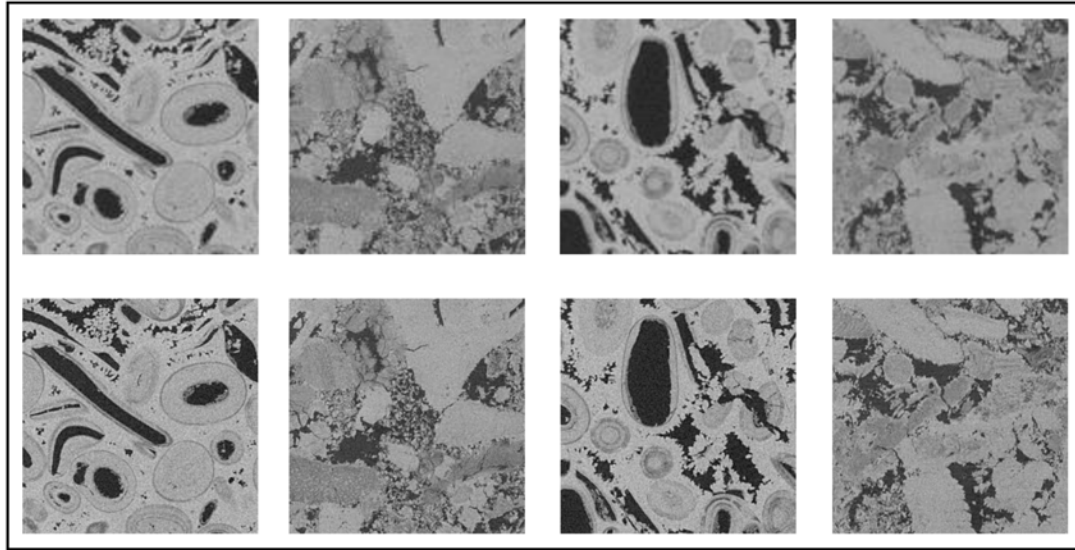


Figure 4—Samples of the image dataset. The first row represents four low-resolution images (125×125), and the second row represents the corresponding high-resolution images (500×500), with an upscaling factor of 4.

Step 2 –Network Training: the proposed network is trained for single image super-resolution with an upscaling factor of 4. The input is a pair of low-resolution and the corresponding high-resolution images. We normalize the images to $[-1, 1]$ before feeding them into the network. To stabilize the training process, the Wasserstein GAN with gradient penalty (Gulrajani et al., 2017) is employed here, and a gradient penalty term is added to the discriminator loss, which has the following form

$$L_D = \frac{1}{m} \sum_{i=1}^m \left\{ D(G(I_i^{\text{input}})) - D(I_i^{\text{GT}}) \right\} + \beta_D \frac{1}{m} \sum_{i=1}^m \left\{ [\|\nabla_{\alpha_i} D(\alpha_i)\| - 1]^2 \right\}, \quad (10)$$

the weight of the gradient penalty term $\beta_D = 10$ and $\alpha_i = \varepsilon I_i^{\text{GT}} + (1 - \varepsilon)G(I_i^{\text{input}})$. ε is a random number ranging from 0 to 1. Table 1 summarizes some hyperparameters for training the proposed FSRGAN.

Table 1—The hyperparameters for training the proposed FSRGAN with scSE blocks.

Parameters	Value
Optimizer	Adam
Learning rate of Generator	10^{-4}
Learning rate of Discriminator	10^{-4}
Coefficient of leaky ReLU	0.2
Batch size	2
Epoch	200
Number of discriminator updates per generator update	2

Step 3 – Quality assessment: The PSNR is used to evaluate the image reconstruction quality. The PSNR is calculated by

$$\text{PSNR} = 10 \log_{10} \frac{I^2}{L_{\text{MSE}}}, \quad (11)$$

with $I = 2$. We further compare the pixel difference maps between the generated super-resolution images and the ground truth images. The results indicate that we manage to achieve high agreement between the generated images and the corresponding ground truth.

Results and Discussion

The proposed FSRGAN with scSE blocks is first validated with 400 images. Afterward, a blind test is conducted using another 400 samples. Figure 5 represents the PSNR values for training, validation, and test sets. The PSNR values have a very close range among training, validation, and testing, indicating the network has good stability and predictivity. Figure 6, Figure 7, and Figure 8 compare the generated super-resolution images and the ground-truth high-resolution images in the training, validation, and test datasets, respectively. Each column represents an individual example, and from top to bottom are the low-resolution images (first row), the generated super-resolution images (second row), the ground-truth high-resolution images (third row), and the pixel difference maps between the super-resolution image and the ground-truth image (fourth row). To improve the visualization, the greyscale images are highlighted in color. The minor difference between the super-resolution images and the corresponding ground truth images indicates the good performance of the proposed FSRGAN, even with much fewer residual blocks than the SRGAN. The generated images include detailed structure information with clear and sharp edges, compared to the low-resolution images.

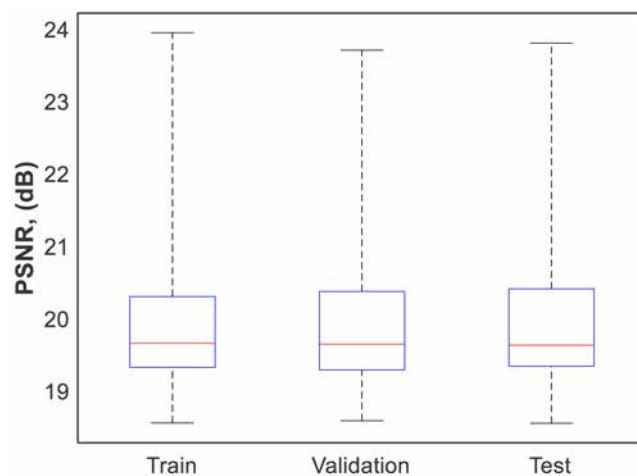


Figure 5—Boxplot of the PSNR value regarding the training, validation, and test set.

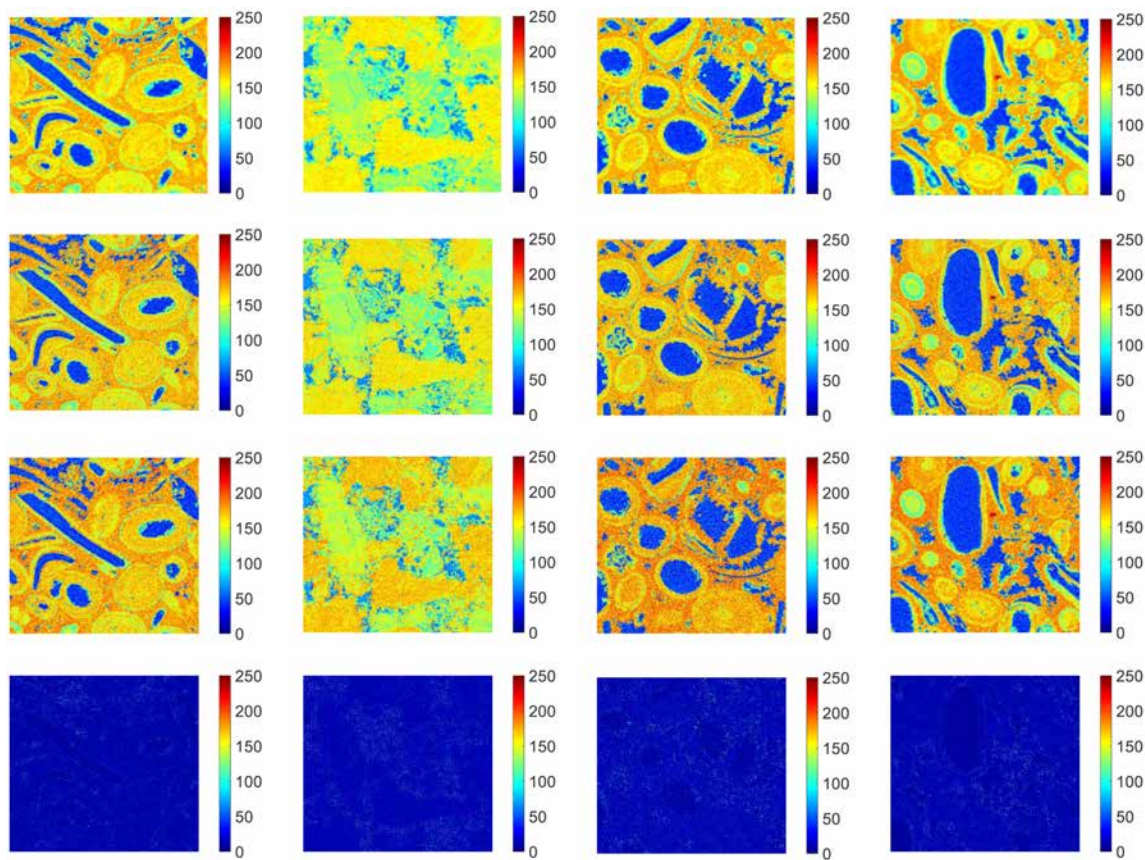


Figure 6—Images from the training set. The first row represents the low-resolution images (125×125), the second row represents the generated super-resolution images (500×500), the third row represents the ground-truth high-resolution images (500×500), and the fourth row represents the difference maps between the generated images and the ground truth.

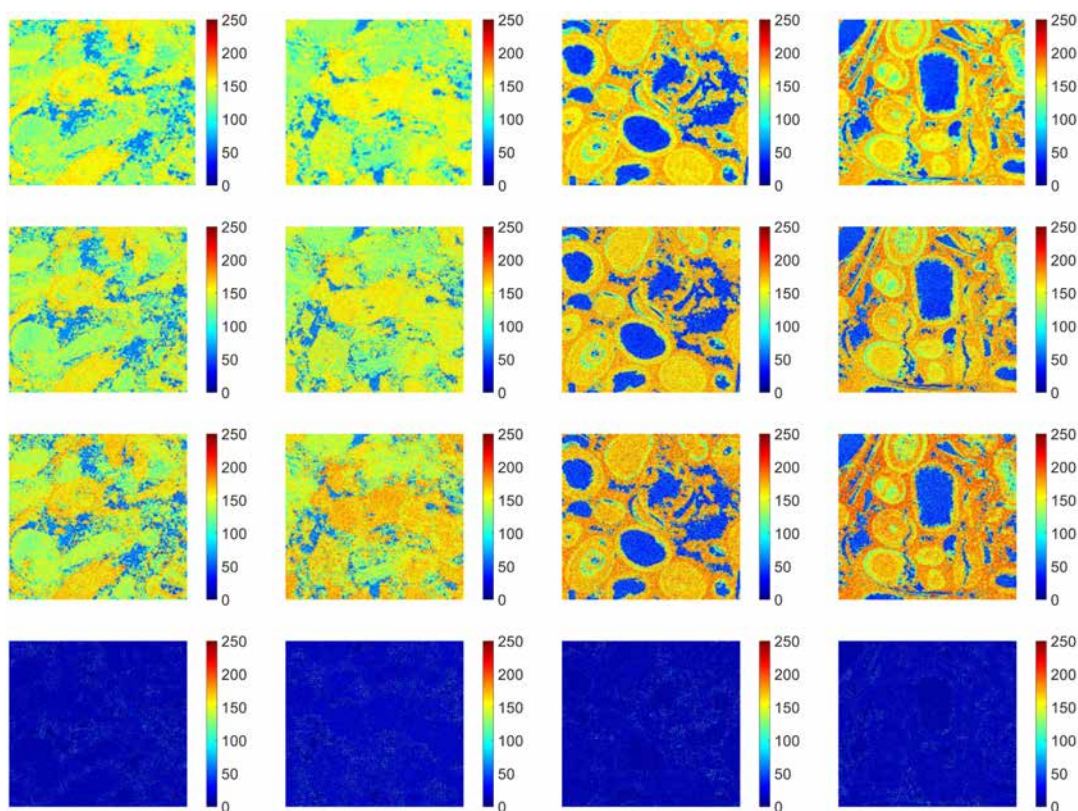


Figure 7—Images from the validation set. The image layout is the same as in Figure 6.

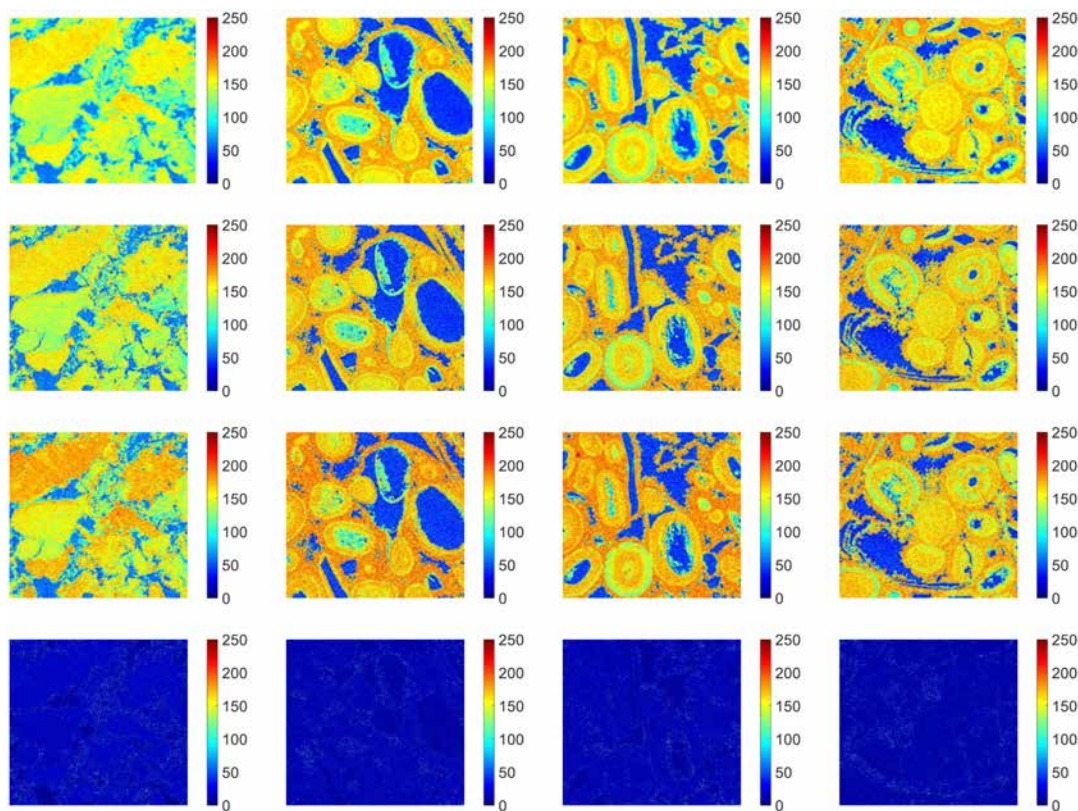


Figure 8—Images from the test set. The image layout is the same as in Figure 6.

Conclusions

This study presents an FSRGAN to enhance the resolution of μ -CT images for carbonate rocks. The proposed network leverages the FSRCNN as the generator network and the scSE block to recalibrate features in spatial and channel dimensions and improve gradient flows. A VGG19 network is used to extract high-level features from which the perceptual loss is evaluated to enhance the perceptual similarity between the generated super-resolution images and the ground-truth high-resolution images. Furthermore, the Wasserstein GAN with gradient penalty is applied to stabilize the training process.

The performance of the proposed FSRGAN with scSE blocks is examined by comparing the difference maps between the generated images and the ground-truth images. Numerical results demonstrate that the proposed network can successfully capture detailed structures of the carbonate rocks and microporous mineralized features. For the carbonate rock images under study, the well-trained generator exhibits a stable performance, but an external test is needed to demonstrate the effectiveness of the FSRGAN further. In addition, using 2D images cannot accurately capture the vertical connection of the digital rock. Therefore, our future work will extend to the reconstruction of high-resolution 3D digital rocks using the super-resolved μ -CT images and SEM images.

Acknowledgment

We want to thank Saudi Aramco for funding this research and thank King Abdullah University of Science and Technology (KAUST) for providing a license for MATLAB. We also acknowledge the Digital Rocks Portal (<https://www.digitalrockportal.org/projects/>) for providing images that were used in this paper.

References

- Albattat, R., He, X., AlSinan, M., Kwak, H., & Hoteit, H. (2022). Modeling Lost-Circulation in Fractured Media Using Physics-Based Machine Learning. 83rd EAGE Annual Conference & Exhibition.
- Alhubail, A., He, X., AlSinan, M., Kwak, H., & Hoteit, H. (2022). Extended Physics-Informed Neural Networks for Solving Fluid Flow Problems in Highly Heterogeneous Media. International Petroleum Technology Conference.
- Andrä, H., Combaret, N., Dvorkin, J., Glatt, E., Han, J., Kabel, M., Keehm, Y., Krzikalla, F., Lee, M., & Madonna, C. (2013). Digital rock physics benchmarks—Part II: Computing effective properties. *Computers & Geosciences*, **50**, 33–43.
- Bai, Y., Berezovsky, V., & Popov, V. (2020a). Digital Rock Core Images Super Resolution via SRCNN Based on Accelerated Bicubic Interpolation. Proceedings of the 2nd International Conference on Industrial Control Network And System Engineering Research, 77–83.
- Bai, Y., Berezovsky, V., & Popov, V. (2020b). Super Resolution for Digital Rock Core Images via FSRCNN. Proceedings of the 2020 4th High Performance Computing and Cluster Technologies Conference & 2020 3rd International Conference on Big Data and Artificial Intelligence, 78–81.
- Chen, H., He, X., Teng, Q., Sheriff, R. E., Feng, J., & Xiong, S. (2020). Super-resolution of real-world rock microcomputed tomography images using cycle-consistent generative adversarial networks. *Physical Review E*, **1012**, 023305.
- Coenen, J., Tchouparova, E., & Jing, X. (2004). Measurement parameters and resolution aspects of micro X-ray tomography for advanced core analysis. Proceedings of International Symposium of the Society of Core Analysts.
- Dong, C., Loy, C. C., He, K., & Tang, X. (2015). Image super-resolution using deep convolutional networks. *IEEE Transactions on Pattern Analysis and Machine Intelligence*, **382**, 295–307.
- Dong, C., Loy, C. C., & Tang, X. (2016). Accelerating the super-resolution convolutional neural network. European Conference on Computer Vision, 391–407.
- Ferrand, L. A., & Celia, M. A. (1992). The effect of heterogeneity on the drainage capillary pressure-saturation relation. *Water Resources Research*, **283**, 859–870.
- Flannery, B. P., Deckman, H. W., Roberge, W. G., & D'Amico, K. L. (1987). Three-dimensional X-ray microtomography. *Science*, **237**, 1439–1444.
- Goodfellow, I., Pouget-Abadie, J., Mirza, M., Xu, B., Warde-Farley, D., Ozair, S., Courville, A., & Bengio, Y. (2014). Generative adversarial nets. *Advances in Neural Information Processing Systems*, **27**.
- Gulrajani, I., Ahmed, F., Arjovsky, M., Dumoulin, V., & Courville, A. C. (2017). Improved training of wasserstein gans. *Advances in Neural Information Processing Systems*, **30**.

- He, X., Qiao, T., Santoso, R., Hoteit, H., AlSinan, M., & Kwak, H. (2021c). Gas Injection Optimization Under Uncertainty in Subsurface Reservoirs: An Integrated Machine Learning-Assisted Workflow. ARMA/DGS/SEG 2nd International Geomechanics Symposium.
- He, X., Santoso, R., Alsinan, M., Kwak, H., & Hoteit, H. (2021b). Constructing Dual-Porosity Models from High-Resolution Discrete-Fracture Models Using Deep Neural Networks. SPE Reservoir Simulation Conference.
- He, X., Santoso, R., & Hoteit, H. (2020). Application of machine-learning to construct equivalent continuum models from high-resolution discrete-fracture models. International Petroleum Technology Conference.
- He, X., Zhu, W., AlSinan, M., Kwak, H., & Hoteit, H. (2022). CO₂ Storage Capacity Prediction In Deep Saline Aquifers: Uncertainty and Global Sensitivity Analysis. International Petroleum Technology Conference.
- He, X., Zhu, W., Santoso, R., Alsinan, M., Kwak, H., & Hoteit, H. (2021). Fracture Permeability Estimation Under Complex Physics: A Data-Driven Model Using Machine Learning. SPE Annual Technical Conference and Exhibition.
- He, X., Zhu, W., Santoso, R., Alsinan, M., Kwak, H., & Hoteit, H. (2021a). CO₂ Leakage Rate Forecasting Using Optimized Deep Learning. SPE Annual Technical Conference and Exhibition.
- Hu, J., Shen, L., & Sun, G. (2018). Squeeze-and-excitation networks. Proceedings of the IEEE Conference on Computer Vision and Pattern Recognition, 7132–7141.
- Johnson, J., Alahi, A., & Fei-Fei, L. (2016). Perceptual losses for real-time style transfer and super-resolution. European Conference on Computer Vision, 694–711.
- Karimpouli, S., & Tahmasebi, P. (2019). Segmentation of digital rock images using deep convolutional autoencoder networks. *Computers & Geosciences*, **126**, 142–150.
- Ledig, C., Theis, L., Huszar, F., Caballero, J., Cunningham, A., Acosta, A., Aitken, A., Tejani, A., Totz, J., & Wang, Z. (2017). Photo-realistic single image super-resolution using a generative adversarial network. Proceedings of the IEEE Conference on Computer Vision and Pattern Recognition, 4681–4690.
- Li, Y., He, X., Zhu, W., AlSinan, M., Kwak, H., & Hoteit, H. (2022). Digital Rock Reconstruction Using Wasserstein GANs with Gradient Penalty. International Petroleum Technology Conference.
- Lim, B., Son, S., Kim, H., Nah, S., & Mu Lee, K. (2017). Enhanced deep residual networks for single image super-resolution. Proceedings of the IEEE Conference on Computer Vision and Pattern Recognition Workshops, 136–144.
- Mosser, L., Dubrule, O., & Blunt, M. J. (2017). Reconstruction of three-dimensional porous media using generative adversarial neural networks. *Physical Review E*, **96**(4), 043309.
- Mostaghimi, P., Blunt, M. J., & Bijeljic, B. (2013). Computations of absolute permeability on micro-CT images. *Mathematical Geosciences*, **45**(1), 103–125.
- Niu, Y., da Wang, Y., Mostaghimi, P., McClure, J. E., Yin, J., & Armstrong, R. T. (2021). Geometrical-based generative adversarial network to enhance digital rock image quality. *Physical Review Applied*, **15**(6), 064033.
- Niu, Y., Mostaghimi, P., Shabaninejad, M., Swietojanski, P., & Armstrong, R. T. (2020). Digital rock segmentation for petrophysical analysis with reduced user bias using convolutional neural networks. *Water Resources Research*, **56**(2), e2019WR026597.
- Roy, A. G., Navab, N., & Wachinger, C. (2018). Recalibrating fully convolutional networks with spatial and channel "squeeze and excitation" blocks. *IEEE Transactions on Medical Imaging*, **37**(2), 540–549.
- Santoso, R., He, X., Alsinan, M., Kwak, H., & Hoteit, H. (2021). Bayesian Long-Short Term Memory for History Matching in Reservoir Simulations. SPE Reservoir Simulation Conference.
- Santoso, R., He, X., & Hoteit, H. (2019). Application of machine-learning to construct simulation models from high-resolution fractured formation. Abu Dhabi International Petroleum Exhibition & Conference.
- Shams, R., Masihi, M., Boozarjomehry, R. B., & Blunt, M. J. (2020). Coupled generative adversarial and auto-encoder neural networks to reconstruct three-dimensional multi-scale porous media. *Journal of Petroleum Science and Engineering*, **186**, 106794.
- Tadjeer, A., Hong, A., & Bratvold, R. B. (2021). Machine learning based decline curve analysis for short-term oil production forecast. *Energy Exploration & Exploitation*, **39**(5), 1747–1769.
- Wang, X., Yu, K., Wu, S., Gu, J., Liu, Y., Dong, C., Qiao, Y., & Change Loy, C. (2018). Esrgan: Enhanced super-resolution generative adversarial networks. Proceedings of the European Conference on Computer Vision (ECCV) Workshops, 0.
- Wang, Y. da, Armstrong, R. T., & Mostaghimi, P. (2019). Enhancing resolution of digital rock images with super resolution convolutional neural networks. *Journal of Petroleum Science and Engineering*, **182**, 106261.
- Wang, Y. da, Armstrong, R. T., & Mostaghimi, P. (2020). Boosting resolution and recovering texture of 2D and 3D micro-CT images with deep learning. *Water Resources Research*, **56**(1), e2019WR026052.
- Wang, Y. da, Arns, J.-Y., Rahman, S. S., & Arns, C. H. (2018). Three-dimensional porous structure reconstruction based on structural local similarity via sparse representation on micro-computed-tomography images. *Physical Review E*, **98**(4), 043310.
- Wang, Y. da, Mostaghimi, P., & Armstrong, R. (2019). A diverse super resolution dataset of sandstone, carbonate, and coal (deeprock-sr).

Wang, Y., & Sun, S. (2021). Multiscale pore structure characterization based on SEM images. *Fuel*, **289**, 119915.